CANCER

Optical microscopy predictions of focal recurrence in glioblastoma

Sanjeev Herr[1,2], Niels Olshausen[2], Melike Pekmezci[3], Jasleen Kaur[2], Youssef Sibih[2], Vardhaan Ambati[2], Abraham Dada[2], Katie Scotford[2], Amit Persad[2], Thiebaud Picart[2], Akhil Kondepudi[4], Gabrielle Malte[2], Gabriella Vulakh[2], Johanna Pechmann[5], Jessica Makolli[5], Nancy Ann Oberheim-Bush[2,6], Albert Kim[7], Jacob Young[2], Mitchel S. Berger[2], Ammar Mallouhi[8], Barbara Kiesel[5], Georg Widhalm[5], Lisa Körner[5], Madhumita Sushil[2], Todd Hollon[4]†, Shawn L. Hervey-Jumper[2,9]*†

A hallmark of glioblastoma (GBM) is disease recurrence that occurs in all patients despite resection, radiation, and chemotherapy. A critical challenge in GBM treatment is the management of recurrent disease for which no standard of care exists. Predicting the location of GBM recurrence may improve the efficiency of advanced-stage therapies. We present an artificial intelligence (AI)–based model to predict the recurrence risk of unprocessed surgical tissues at initial resection. AI-informed label-free optical microscopy was used to generate a normalized tumor infiltration value (AI-infiltration) for optical images of samples taken from resection cavity margins. These values, in combination with clinical, radiographic, and molecular variables, were used to build a predictive model of focal recurrence. In a cohort of 80 patients, comprising 367 samples and 133,454 unique images, GBM infiltration was significantly higher in margin samples from recurrent sites ($P = 0.03$) compared with those from nonrecurrent sites. A random forest machine learning classifier predicted site recurrence with an average area under the receiver operating characteristic curve of 87% ± 10.0 for the training cohort and 80% (95% confidence interval: 0.64 to 0.97) for the validation cohort. AI-infiltration was the strongest contributor to recurrence prediction, outperforming tumor molecular features. Model performance remained high regardless of tumor location, resulting in random forest model predictions of recurrence at 5 and 10 millimeters of each sample. These findings represent the potential of AI to predict sites of tumor recurrence, thereby improving accessibility to targeted, precision, and multimodal therapy for the highest-risk areas of disease.

INTRODUCTION

Focal recurrence of cancer after initial standard-of-care therapies is one underlying cause of the high mortality associated with solid organ malignancies. Recurrence is particularly challenging to manage for patients with glioblastoma (GBM), which is a universally fatal disease with a median overall survival of 17 months (*1*). Standard-of-care treatment at initial diagnosis includes maximum safe resection followed by concomitant radiation and chemotherapy, which improves overall survival; however, these therapies are not durable because nearly all patients experience recurrence (*2*–*4*). Management of later stages of the disease, after initial treatments fail, is a fundamental challenge affecting patient survival without effective therapies over the past two decades. An estimated 130 clinical trials have been unable to show efficacy for patients with recurrent GBM, with an associated cost of more than 1.5 billion US dollars (*5*, *6*).

GBM recurrence presents at or near the resection cavity margins in three of four patients (*1*, *4*, *7*). Several structural and metabolic imaging methods have been developed to estimate tumor recurrence once it has occurred and is radiographically evident (*8*). However, given the proximity of tumor recurrence to the primary disease site in most patients, quantifying microscopic tumor infiltration at the surgical margin has the potential to forecast future recurrence. Conventional histology of clinical samples is both time- and labor-intensive, limiting scalability (*9*–*12*). Artificial intelligence (AI) estimates of GBM infiltration using unprocessed surgical tissues address this limitation by combining optical microscopy [stimulated Raman histology (SRH)] with visual foundation models trained on a dataset of more than 11,000 brain tumor tissue specimens (*13*–*21*). Here, we aim to develop a predictor of GBM recurrence using an open-source, AI-based tumor-infiltration model, called FastGlioma, which is measured from tumor margin samples acquired during initial surgical resection. A population of patients with GBM and with and without recurrence was used to train an AI model to predict recurrence within 5 and 10 mm of each sampled site. Tissue samples from GBM resection margins may provide physicians with clinically actionable information that forecasts future recurrence, paving the way for targeted, precision medicine, tumor-directed therapies at late stages of disease when no standard of care exists.

RESULTS

Patient population and characteristics

Between May 2022 and March 2025, a multinational, multicenter patient cohort was generated from patients with IDH–wild-type GBM that underwent tumor resection and tumor margin sampling with

[1]Drexel University College of Medicine, Philadelphia, PA 19129, USA. [2]Department of Neurological Surgery, University of California, San Francisco, San Francisco, CA 94143, USA. [3]Department of Pathology, University of California, San Francisco, San Francisco, CA 94143, USA. [4]Machine Learning in Neurosurgery Laboratory, Department of Neurosurgery, University of Michigan, Ann Arbor, MI 48105, USA. [5]Department of Neurosurgery, Medical University of Vienna, Vienna, Austria. [6]Department of Neurology, University of California, San Francisco, San Francisco, CA 94143, USA. [7]Department of Neurological Surgery, Washington University School of Medicine, St. Louis, MO 63110, USA. [8]Department of Biomedical Imaging and Image-guided Therapy, Medical University of Vienna, Vienna, Austria. [9]Weill Institute of Neurosciences, University of California, San Francisco, San Francisco, CA 94158, USA.
*Corresponding author. Email: shawn.hervey-jumper@ucsf.edu
†These authors contributed equally to this work.

spatial annotation of tissue specimens for analysis of histopathology and stimulated Raman histology (SRH) imaging. The entire cohort consisted of 84 patients, 60 patients from the University of California, San Francisco (UCSF) and 24 patients from the Medical University of Vienna. While the distribution of margin samples differed between institutions (fig. S2A), no differences in progression free survival were identified between institutions when analyzing patients with tumor margin samples with under 25, 26 to 50%, and 51 to 75% (fig. S2B). Given concern for institution sampling biases, the remainder of our analyses were conducted on development datasets within the UCSF cohort with an additional prospective internal validation cohort of another 20 patients from the UCSF health system.

Within the UCSF training cohort of 60 patients, 43 GBMs recurred on the basis of Response Assessment in Neuro-Oncology (RANO) 2.0 criteria (Fig. 1A). No significant difference in demographic (sex and age), clinical (adjuvant chemoradiation), or radiographic (tumor volume, FLAIR volume, and extent of resection) features were identified between cohorts (Fig. 1A and Table 1). Patients whose tumors recurred showed a significantly greater percentage of TP53 mutations compared to those who had not recurred (47 versus 18%, $P = 0.05$, Fisher's exact).

Margin sample characterization and recurrence model training

Fresh tissue specimens were sampled at the surgical margins of resection cavities to estimate microscopic GBM infiltration using SRH (Fig. 1B) (*17*, *21*). Label-free optical imaging was performed via SRH on surgical specimens, with image contrast generated from the intrinsic biochemical properties of the specimen, bypassing the need for tissue dyes or stains. A GBM infiltration score was acquired from the SRH foundation model FastGlioma, called AI-infiltration, which was built on the basis of tissues from 13 medical centers and included imaging data from more than 3000 patients spanning the diagnostic spectrum of central nervous system tumors (*21*). The FastGlioma model uses a linear slide scoring layer to output a single scalar value between 0 and 1 that indicates the degree of tumor infiltration within a whole-slide SRH image. Model training for detecting early sites of focal recurrence was conducted on 60 patients containing 273 samples, with the median number of sites sampled at the margin per patient being 4.5 (3.0 to 5.0), with no significant difference in sample number between recurred and nonrecurring cohorts (Table 1). The recurrent cohort of patients had a median time to recurrence of 5.5 months (3.0 to 9.3). Using expert-guided manual inspection, samples were determined to be recurrent or nonrecurrent. By comparing intraoperative navigation screenshots, postoperative imaging, and imaging at the time of recurrence, 59 sample sites were determined to be sites of recurrence, and 214 were nonrecurrent sites.

Margin samples, taken from regions directly proximal to the tumor or resection cavity, were spatially mapped in three-dimensional (3D) space by calculating the Euclidean distance between each patient's core sample (used as a reference coordinate) and their respective margin samples (Fig. 1C). This approach was used to standardize relative spatial positioning across patients. Visual inspection of this plot demonstrated a widespread distribution of samples around each resection cavity without significant sample clustering. Kernel density plots demonstrated unimodal and approximately symmetric distribution of samples in the *x*, *y*, and *z* axes, further supporting a normal distribution of samples (Fig. 1D). To further assess sample distribution, the average SD from pairwise distances between margin samples was used as a measure of variability in sample dispersion (fig. S4A). Between patients who recurred and those who did not, there was no significant difference in the degree of sample dispersion indicating a comparable distribution of samples within patients between cohorts (nonrecurrent: 17 ± 5.7 mm; recurrent: 17 ± 5.4 mm; $P = 0.98$, independent *t* test). To assess the potential bias of recurrent samples being taken closer to the core and thus having an expected higher degree of infiltration, the distance for each margin sample to its respective core sample was calculated (fig. S4B). When this distance was compared between samples that recurred and those that did not recur, there was no significant difference [nonrecurrent: 29 mm (21 to 39); recurrent: 32 mm (22 to 44), $P = 0.18$, Wilcoxon rank-sum test].

GBM infiltration scoring

Neuropathologist coauthor M.P. analyzed tissue obtained from resection cavity margins using histologic and optical microscopy techniques to determine the influence of tumor infiltration on recurrence. Neuropathologist assessment using hematoxylin and eosin (H&E) and p53 staining ranked the degree of tumor infiltration within each sample (termed path-infiltration). In cases that were p53–wild type, tumor cells were identified on the basis of morphology (i.e., enlarged nuclei, irregular nuclear borders, hyperchromasia, etc.) on routine H&E-stained slides. Path infiltration within each sample was annotated for ordinal metric learning using a validated four tier scale: (0) normal brain tissue/no tumor; (1) atypical cells/possible tumor but not definitive; (2) sparse tumor infiltration; (3) dense tumor infiltration (*21*) (Fig. 2A). Tumor samples for path-infiltration comprised a dataset of 32 core samples from 32 patients with 137 margin samples. AI-informed label-free optical microscopy was used to generate a normalized tumor infiltration value (termed AI-infiltration) for whole-slide optical images of samples taken from resection cavity margins based on the recently published FastGlioma model (*21*). The relationship between pathologist-annotated tissue infiltration (path infiltration) and AI-infiltration across groups demonstrated an infiltration correlation across measures (Fig. 2B). The median AI-infiltration for ordinal assigned pathologist infiltration samples was: 0, no tumor identified = 0.31 (0.22 to 0.45); 1, atypical cells = 0.38 (0.28 to 0.54); 2, sparse tumor infiltration = 0.68 (0.55 to 0.84); and 3, dense tumor infiltration = 0.93 (0.88 to 0.98). Pairwise Wilcoxon rank-sum tests with Bonferroni correction were performed to compare median infiltration for each histopathology group. Significant differences were observed between 0 and 2 ($P = 1.9 \times 10^{-7}$), 0 and 3 ($P = 2.0 \times 10^{-11}$), 1 and 2 ($P = 8.7 \times 10^{-11}$), 1 and 3 ($P = 1.3 \times 10^{-8}$), and 2 and 3 ($P = 5.4 \times 10^{-6}$), while no significant difference was found between groups 0 and 1 ($P = 1.0$).

To confirm that all tumor core samples demonstrated infiltrative tumor cells, the distribution of path infiltration was compared between core samples and margin samples (Fig. 2C). Samples taken from the core showed a significantly higher median infiltration of tumor cells compared to margin samples [core: 3 (3 to 3); margin: 2 (1 to 2), $P = 5.0 \times 10^{-11}$, Wilcoxon rank-sum test]. To define the relationship between infiltration and recurrence at the sample (not patient) level, margin samples were separated into cohorts of samples that recurred ($n = 38$) and those that did not recur ($n = 99$). Tumor margin samples that recurred demonstrated a significantly greater extent of infiltration defined histologically (nonrecurrent samples median score: 2 (0 to 2), skewness: −0.40; recurrent samples

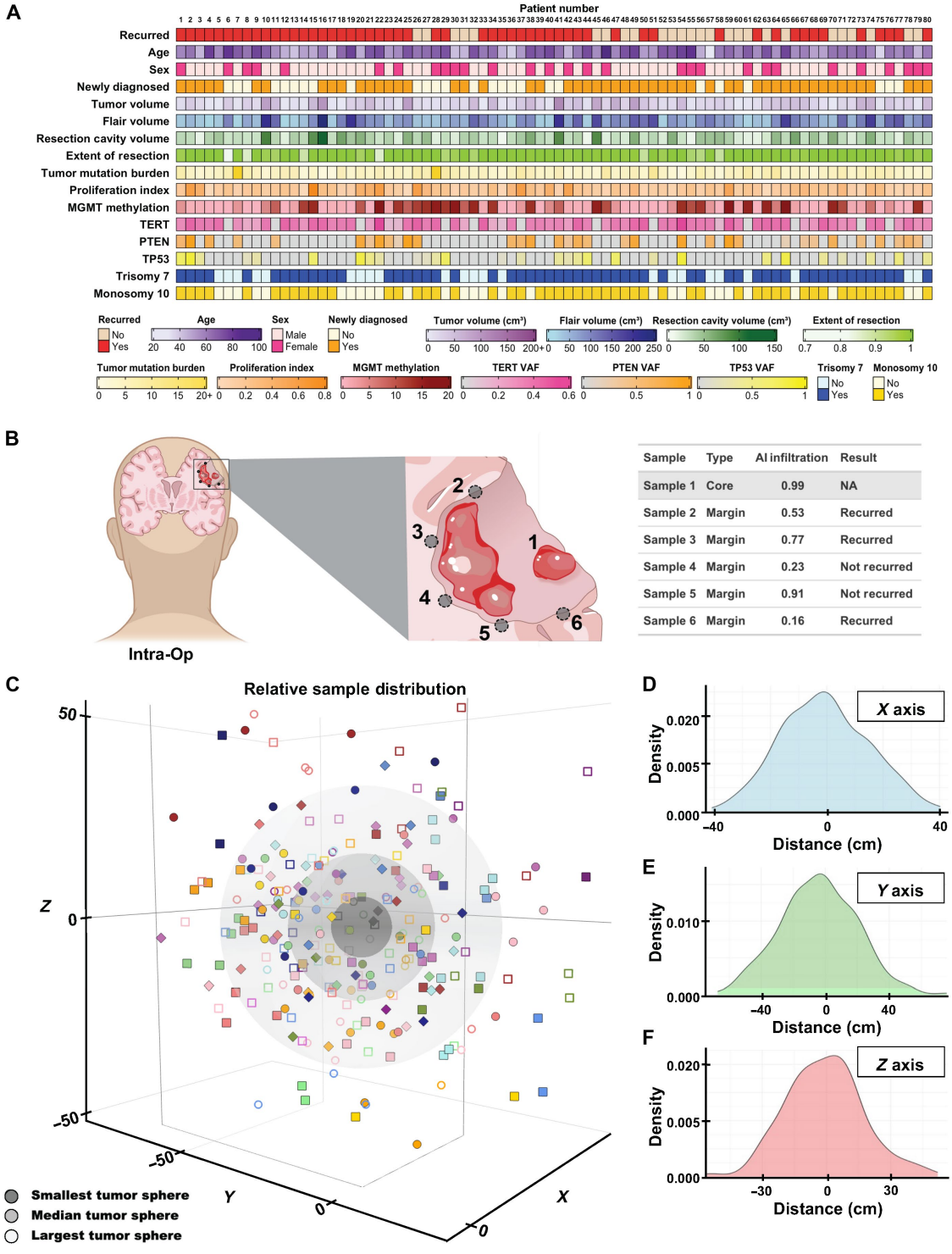

Fig. 1. Patient and sample characteristics for the training cohort. (**A**) Oncoprint detailing individual patient characteristics for the entire UCSF training cohort ($n = 60$), including clinical, radiographic, and molecular features. (**B**) Schematic representation of the study workflow in which patients undergoing resection have one sample taken from the tumor core and varying samples taken at the margins, analyzed at the pixel level using SRH. The output for each sample is an infiltration value. Illustration credit: N. Sirivansanti. (**C**) Relative distribution of each patient's margin samples in relation to their tumor using Euclidean distances, plotted with the smallest, median, and largest tumor volumes visually represented. (**D**) Kernel density plots demonstrating unipolar and approximately symmetric distribution of samples centered around 0 in *x*, *y*, and *z* axes.

Table 1. Patient demographics and oncologic characteristics of the training cohort.

	Total	Recurred	Non recurred	*P* value
	(*n* = 60)	(*n* = 43)	(*n* = 17)	
Sex				1.00
Male (%)	40 (67%)	29 (67%)	11 (65%)	
Female (%)	20 (33%)	14 (33%)	6 (35%)	
Mean age (years ± SD)	60 ± 13	59 ± 12	62 ± 15	0.45
Newly diagnosed (%)	38 (63%)	25 (58%)	13 (77%)	0.24
Tumor volume (cm^3)	18 (9.4–31)	18 (7.0–32)	19 (9.6–30)	0.84
Flair volume (cm^3)	79 (35–120)	75 (32–120)	81 (46–120)	0.57
Resection cavity volume (cm^3)	30.5 (23.0–43.1)	29.6 (23.3–40.3)	35.0 (15.8–44.8)	1.00
Extent of resection (%)	100 (97–100)	100 (98–100)	100 (97–100)	0.36
Adjuvant chemoradiation (%)	57 (95%)	41 (95%)	16 (94%)	1.00
Follow-up time (months ± SD)	11 ± 6.7	9.7 ± 6.3	14 ± 6.8	0.02
Number of margin samples	4.5 (3.0–5.0)	5 (3.0–6.0)	4 (4.0–5.0)	0.48
Tumor molecular features (%)				
MGMT methylation	42 (70%)	28 (65%)	14 (82%)	0.23
TERT mutation	52 (87%)	37 (86%)	15 (88%)	1.00
TP53 mutation	23 (38%)	20 (47%)	3 (18%)	0.05
Trisomy 7	41 (68%)	29 (67%)	12 (71%)	1.00
Monosomy 10	37 (62%)	26 (61%)	11 (65%)	0.99

Table 2. Classifier screening performance and variable importance.

Classifier	Logistic regression	k-Nearest neighbor	Support vector machines	Random Forest	Gradient boosted trees	Xtreme gradient boosted trees
Sensitivity	0.61	0.71	0.67	0.65	0.65	0.70
Specificity	0.71	0.61	0.83	0.88	0.87	0.84
PPV	0.36	0.34	0.53	0.60	0.58	0.54
NPV	0.87	0.89	0.90	0.90	0.90	0.91
CV mean AUC (± SD)	0.77 ± 0.12	0.82 ± 0.12	0.85 ± 0.12	0.87 ± 0.10	0.85 ± 0.12	0.86 ± 0.11
Pooled AUC	0.74	0.74	0.81	0.84	0.84	0.85
Validation AUC	0.77	0.62	0.49	0.80	0.66	0.70
Variable weights						
Newly diagnosed	1.25	1.02	1.58	9.73	31.8	0.037
Resection cavity volume	0.997	1.05	1.80	17.0	47.1	0.154
Extent of resection	1.01	1.00	1.22	6.51	13.8	0.028
TERT mutation	0.999	1.03	1.73	12.5	22.6	0.057
MGMT methylation	1.15	0.984	1.19	12.1	23.0	0.073
Trisomy 7	1.39	1.00	1.27	2.45	3.85	0.003
PTEN mutation	1.17	1.08	1.25	9.33	15.4	0.053
TP53 mutation	1.01	1.02	1.19	6.69	3.19	0.020
AI-infiltration	1.06	1.10	2.43	20.1	50.8	0.165
Tumor mutation burden	1.01	0.976	1.08	10.2	25.4	0.023
Age	1.04	1.03	1.28	17.1	39.4	0.081
Flair volume	1.46	1.00	1.24	13.1	41.6	0.115
Monosomy 10	1.83	1.02	1.37	2.85	4.88	0.031
Proliferation index	1.02	0.992	1.21	11.8	9.54	0.048
Tumor volume	1.56	1.07	1.26	13.9	31.8	0.106
Sex	1.01	1.00	1.29	2.46	0.223	0.005

Table 3. Variable importance ranking and model performance of reverse feature elimination.

Iteration	1	2	3	4	5	6	7	8	9	10	11	12	13	14	15	16
Variable importance ranking																
AI-infiltration	1st	1st	1st	1st	1st	1st	1st	1st	1st	1st	1st	1st	1st	1st	2nd	
Age	2nd	2nd	2nd	2nd	2nd	2nd	3rd	2nd	2nd	3rd	2nd	3rd	3rd	3rd		
Resection cavity volume	3rd	3rd	3rd	3rd	3rd	3rd	2nd	3rd	3rd	2nd	3rd	2nd	2nd	2nd	1st	1st
Tumor volume	4th	4th	4th	5th	4th	4th	6th	6th	4th	6th	4th	4th	4th			
Flair volume	5th	5th	5th	4th	5th	6th	5th	7th	7th	5th	5th	5th				
TERT mutation	6th	6th	6th	6th	6th	5th	4th	4th	6th	4th	6th					
MGMT methylation	7th	7th	7th	7th	7th	7th	7th	9th								
Proliferation index	8th	8th	8th	8th	9th	8th	8th	8th	5th	7th						
Tumor mutation burden	9th	9th	9th	9th	8th	9th	9th	5th	8th							
Newly diagnosed	10th	10th	10th	10th	10th	10th	10th									
PTEN mutation	11th	11th	11th	11th	11th	11th										
TP53 mutation	12th	13th	13th	13th												
Extent of resection	13th	12th	12th	12th	12th											
Monosomy 10	14th	14th	14th													
Trisomy 7	15th	15th														
Sex	16th	19th														
Model performance																
Sensitivity	0.65	0.65	0.65	0.65	0.65	0.64	0.63	0.64	0.64	0.64	0.64	0.64	0.63	0.57	0.42	0.80
Specificity	0.88	0.88	0.88	0.88	0.88	0.88	0.89	0.88	0.88	0.89	0.89	0.89	0.90	0.89	0.85	0.79
PPV	0.60	0.60	0.60	0.60	0.60	0.60	0.60	0.60	0.60	0.61	0.62	0.61	0.63	0.60	0.44	0.51
NPV	0.90	0.90	0.90	0.90	0.90	0.90	0.90	0.90	0.90	0.90	0.90	0.90	0.90	0.88	0.84	0.93
CV mean AUC	0.87	0.86	0.86	0.85	0.86	0.85	0.85	0.85	0.85	0.84	0.84	0.82	0.81	0.81	0.72	0.83
AUC SD	0.10	0.10	0.11	0.12	0.09	0.12	0.11	0.10	0.11	0.12	0.12	0.12	0.13	0.13	0.12	0.14
Pooled AUC	0.84	0.84	0.84	0.84	0.84	0.84	0.84	0.84	0.84	0.83	0.83	0.81	0.80	0.80	0.72	0.83
Validation AUC	0.80	0.77	0.78	0.81	0.79	0.75	0.78	0.74	0.73	0.71	0.55	0.58	0.45	0.54	0.55	0.50
Precision	0.60	0.60	0.60	0.60	0.60	0.60	0.60	0.60	0.60	0.61	0.62	0.61	0.63	0.61	0.62	0.51
Recall	0.65	0.65	0.65	0.65	0.65	0.64	0.63	0.64	0.64	0.64	0.64	0.64	0.63	0.64	0.64	0.80
F1-Score	0.62	0.62	0.63	0.62	0.62	0.62	0.62	0.62	0.62	0.63	0.63	0.63	0.63	0.63	0.63	0.62

median score: 2 (1 to 3), skewness: −0.53, $P = 0.02$, Wilcoxon rank-sum test) (Fig. 2D). These same findings held true when comparing AI-generated infiltration for core ($n = 60$) and margin samples ($n = 273$) as well as recurred ($n = 59$) and nonrecurred samples ($n = 214$). The median AI-infiltration for core samples was significantly higher than that of margin samples [core: 0.95 (0.91 to 0.98); margin: 0.61 (0.41 to 0.87), $P = 8.0 \times 10^{-17}$, Wilcoxon rank-sum test] (Fig. 2E), and the median AI-infiltration in recurrent margin samples was significantly higher than those of margin samples that did not recur (nonrecurrent: 0.60 (0.41 to 0.86); recurrent: 0.74 (0.50 to 0.90), $P = 0.03$, Wilcoxon rank-sum test) (Fig. 2F).

To identify the relationship between infiltration and focal recurrence, logistic regression was performed using path infiltration alone as a predictor (mAUC = 0.59 ± 0.20) and AI-infiltration alone as a predictor (mAUC = 0.62 ± 0.17) (fig. S5). These findings suggest similarities between histopathology and AI-generated GBM infiltration measures in tumor core and margin samples, which individually inadequately predict focal recurrence. Given that a complex interplay of factors, including tumor infiltration, determines solid-organ tumor recurrence, the next step was to build a predictive model of GBM recurrence using infiltration, oncologic, and clinical variables.

Recurrence model training and fine-tuning

Several oncologic and molecular variables are associated with GBM recurrence. However, it remains unknown which features predict focal recurrence. Machine learning models for GBM recurrence were developed, incorporating variables at both the sample and individual patient levels, including AI-infiltration, clinical variables, oncological variables, and targeted next-generation sequencing. Workflow for model selection and training is outlined in fig. S6. Six classifier models were screened using the selected variables: logistic regression (LR), k-nearest neighbors (k-NNs), support vector machines (SVMs), random forest (RF), gradient-boosted trees (GBTs), and extreme GBTs (XGBs) (Fig. 3A). Each model was trained using 10-fold stratified internal cross-validation. RF was the most predictive model for recurrence with an mAUC of 87% ± 10. The recurrence model was subsequently validated using a unique prospective internal cohort of 20 additional patients with GBM, including 98 tumor margin samples, which yielded an AUC of 80% (95% confidence interval:

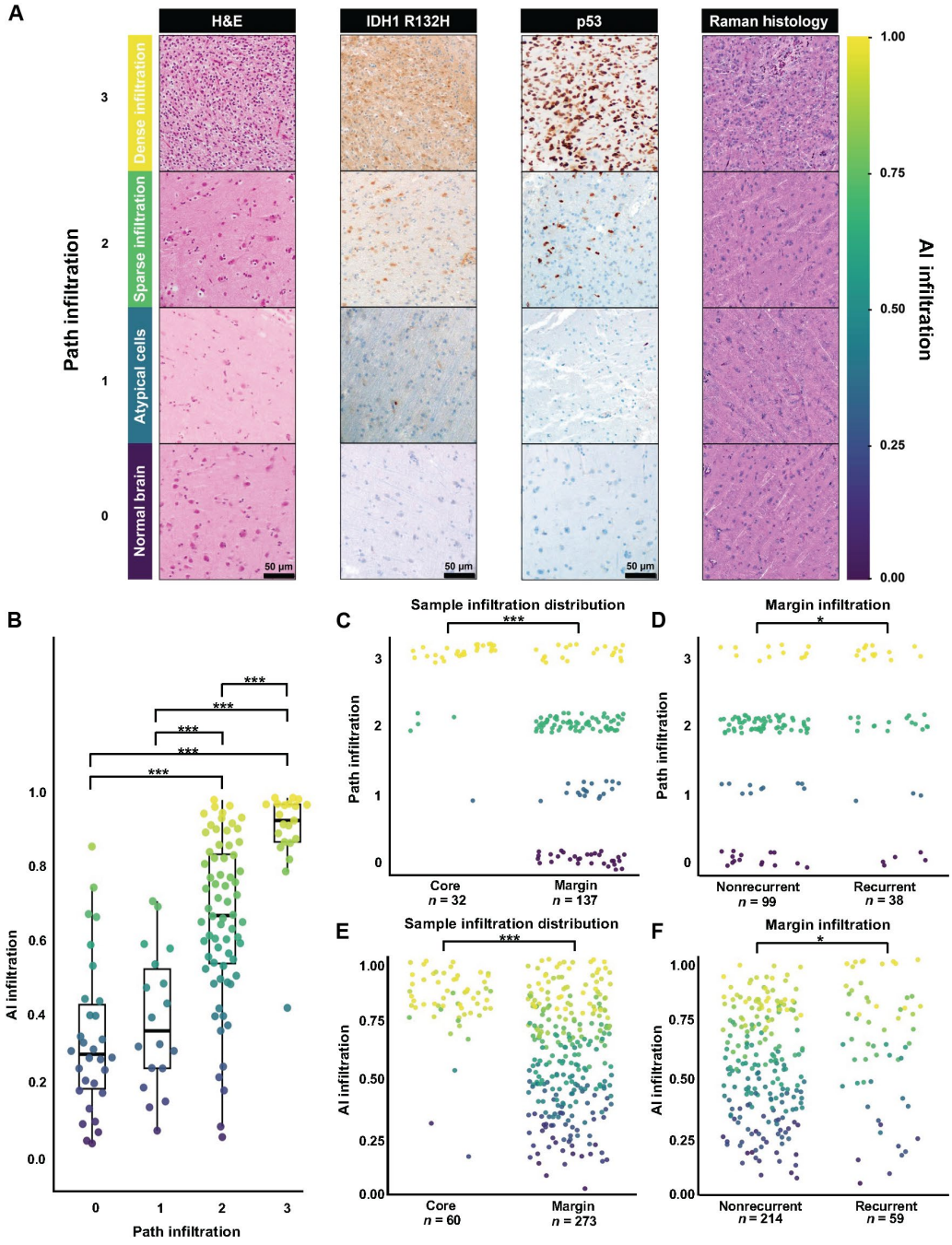

Fig. 2. SRH AI-generated infiltration values correlate with focal GBM recurrence. (**A**) Tumor core ($n = 32$) and margin samples ($n = 137$) were H&E and p53 stained by histopathologists to designate the degree of pathologist defined infiltration using a scale of 0 to 3 (0, normal brain tissue/no tumor; 1, atypical cells/possible tumor; 2, sparse tumor infiltration; 3, dense tumor infiltration). AI-infiltration of each tissue specimen was analyzed using FastGlioma, which was computed using Raman histology (**B**). Comparison of margin sample path infiltration and AI-infiltration demonstrated a correlation with significant differences in median infiltration across histopathology groups [0 = 0.31 (0.22 to 0.45), 1 = 0.38 (0.28 to 0.54), 2 = 0.68 (0.55 to 0.84), and 3 = 0.93 (0.88 to 0.98), pairwise Wilcoxon rank-sum tests with Bonferroni correction]. Significant differences were observed between groups 0 and 2 ($P = 1.9 \times 10^{-7}$), 0 and 3 ($P = 2.0 \times 10^{-11}$), 1 and 2 ($P = 8.7 \times 10^{-11}$), 1 and 3 ($P = 1.3 \times 10^{-8}$), and 2 and 3 ($P = 5.4 \times 10^{-6}$). (**C**) Path infiltration confirmed a significant difference in the median values of core samples and margin samples using Wilcoxon rank-sum test [core: 3 (3-3), margin: 2(1-2), $P = 5.0 \times 10^{-11}$]. (**D**) When split into cohorts of samples that recurred and samples that did not recur, recurrent samples demonstrated a significantly higher infiltration distribution [Nonrecurrent: 2 (0 to 2), skewness: −0.40; recurrent: 2 (1 to 3), skewness: −0.53, $P = 0.02$] using Wilcoxon rank-sum test. In the entire sample set ($n = 273$), Wilcoxon rank-sum testing for AI-infiltration demonstrated similar significant findings with (**E**) increased median infiltration values in core samples [core: 0.95 (0.91 to 0.98), margin: 0.61 (0.41 to 0.87), $P = 8.0 \times 10^{-17}$] and (**F**) increased median infiltration values in recurrent margin samples [nonrecurrent: 0.60 (0.41 to 0.86), recurrent: 0.74 (0.50 to 0.90), $P = 0.03$]. The Raman histology images shown in (A) were obtained from the OpenSRH: Optimizing Brain Tumor Surgery Using Intraoperative Stimulated Raman Histology dataset [Jiang *et al.*, 2022; University of Michigan], available at https://opensrh.mlins.org/. OpenSRH data are licensed under the Creative Commons Attribution-NonCommercial-ShareAlike 4.0 International License (CC BY-NC-SA 4.0; https://creativecommons.org/licenses/by-nc-sa/4.0/). Images were cropped and resized for presentation.

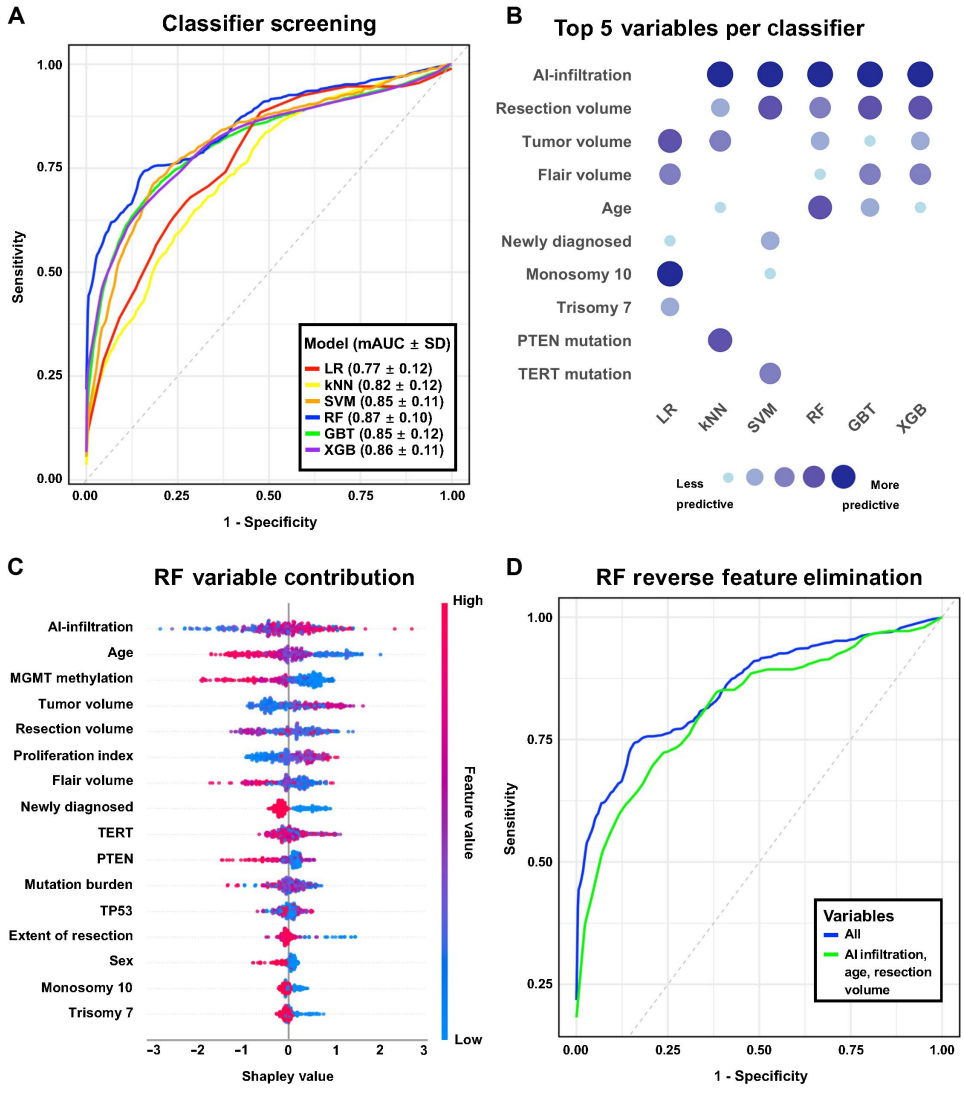

Fig. 3. Classifier screening and model training. (**A**) Ten-fold internal stratified cross-validation was conducted using six different classifier models [LR, kNN, SVM, RF, GBT, and XGB]. RF was identified as the best-performing model with an mAUC of 87% ± 10. (**B**) The top predictors of margin sample recurrence across different classifier models demonstrated that AI-infiltration was the highest contributing variable for five of six models. (**C**) Shapley analysis of the best-performing model demonstrated the directionality and impact of each variable on the model performance. (**D**) Reverse feature elimination on the RF model was used to create the most generalizable model while maintaining clinical utility. This model was determined to use only AI-infiltration, age, and resection cavity volume as variables with a mAUC of 82% ± 12, and AI-infiltration remained the top predictor.

0.64 to 0.97; bootstrapped, 2000 resamples). For each classifier model, feature weighting was conducted, and the contribution of each variable to model performance was analyzed. AI-infiltration was determined to be the single most predictive variable in five of six classifiers tested (Fig. 3B). Shapley additive explanation values for each variable in the RF model identified the contribution and directionality of each variable to model performance (Fig. 3C). AI-infiltration contributed greatly to recurrence prediction with increased infiltration resulting in a higher probability of recurrence and decreased infiltration resulting in a lower probability of recurrence.

Following model selection, the model's generalizability was assessed by determining the minimum effective number of variables required for predicting margin sample recurrence while maintaining clinical utility with an AUC threshold of 80%. This was achieved through manual reverse feature elimination with AUC thresholding, where the lowest-weighted variable was eliminated in each iteration until the minimum number of variables required to maintain the threshold was reached. This revealed that the RF model could predict margin sample recurrence with a minimum of three variables: AI-infiltration, age, and resection cavity volume (AUC = 82% ± 12) (Fig. 3D). We further investigated resection cavity volume as a variable by evaluating its relationship with preoperative tumor volume using linear regression and found a significant association, yet a moderate coefficient of determination (R^2) indicates a multifactorial nature ($\beta = 0.52$, $P < 2.0 \times 10^{-16}$; $R^2 = 0.40$).

Spatial prediction of GBM recurrence

The propensity for GBMs to recur has been attributed to malignant cell subpopulations that are resistant to chemoradiation therapy, which may have a focal regional representation in the brain. Recurrence

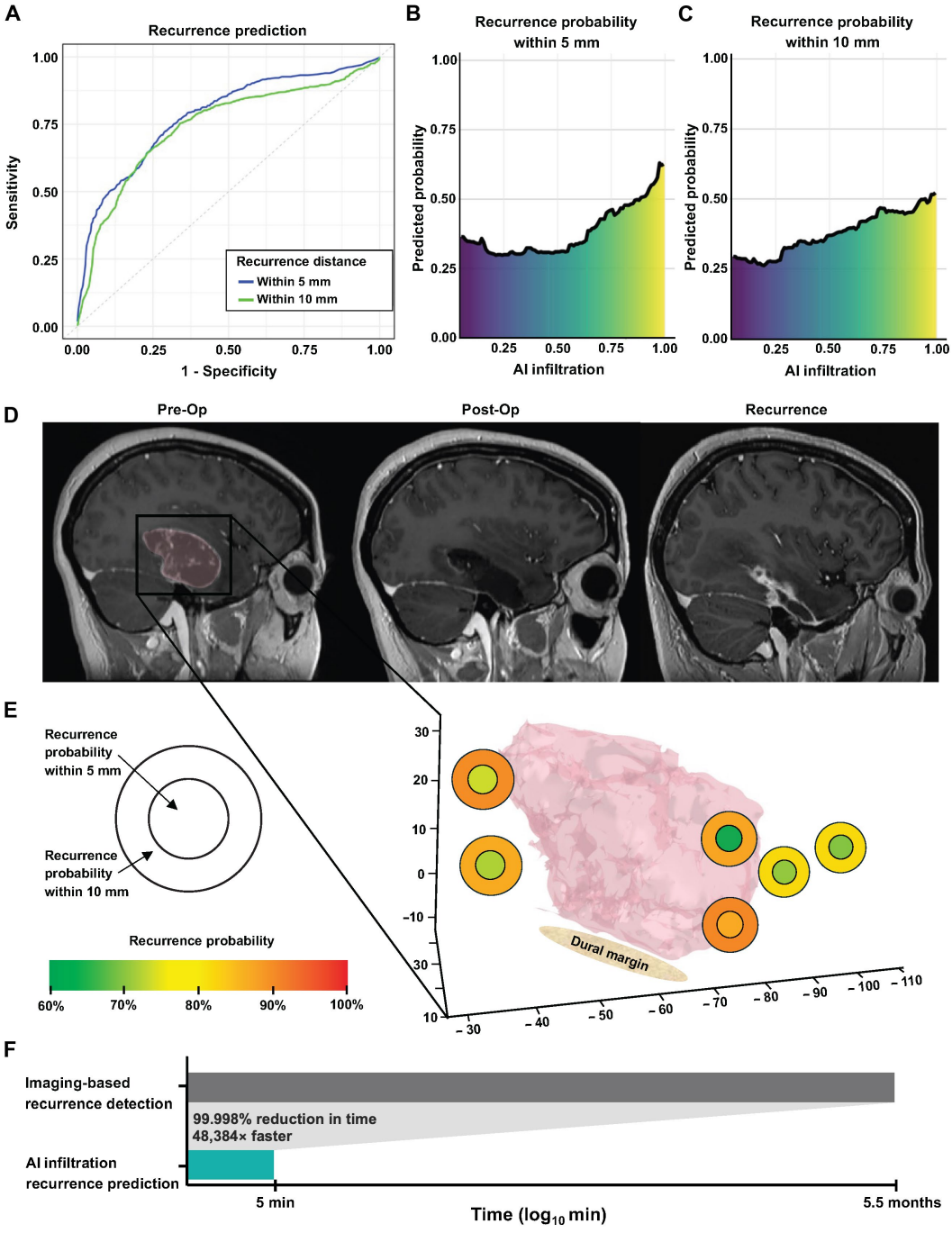

Fig. 4. Localization and prediction of GBM recurrence using AI-infiltration modeling. Location of recurrence for each sample was annotated as within 5 mm or within 10 mm away. (**A**) RF models were built to predict focal recurrence within 5 mm (mAUC: 80% ± 10) and within 10 mm (mAUC: 76% ± 13) from each sample. (**B** and **C**) Partial dependency plots demonstrated the effect of AI-infiltration on recurrence probability within 5 and 10 mm when all other variables were held constant. (**D**) T1 post–gadolinium sagittal MRI from an illustrative patient 24 hours before surgery, 48 hours after surgery, and at the time of recurrence (9 months after resection) are shown. (**E**) Plotted are the patient's tumor, sample locations, and the predicted probabilities of recurrence within 5 mm (P5mm) and within 10 mm (P10mm) (sample 1: AI-infiltration: 0.60, P5mm: 73%, P10mm: 87%; sample 2: AI-infiltration: 0.94, P5mm: 72%, P10mm: 90%; sample 3: AI-infiltration: 0.21, P5mm: 60%, P10mm: 88%; sample 4: AI-infiltration: 0.99, P5mm: 87%, P10mm: 90%; sample 5: AI-infiltration: 0.57, P5mm: 70%, P10mm: 83%; sample 6: AI-infiltration: 0.63, P5mm: 69%, P10mm: 82%). (**F**) AI-infiltration as a marker for focal prediction of recurrence is a method that allows for the prediction of focal recurrence supporting standard imaging-based detection.

models were refined to predict the site of recurrence. To assess our ability to predict the proximity of recurrence in relation to each sample, we used RF classification with the same set of previously selected variables to generate models for the prediction of recurrence within 5 mm of a sample and within 10 mm of a sample. These models performed well for predicting recurrence within 5 mm (mAUC: 80% ± 10) and recurrence within 10 mm (mAUC: 76% ± 13) (Fig. 4A). To understand the contribution of AI-infiltration to the predictability of these models, partial dependency plots were generated, demonstrating the effect of AI-infiltration on recurrence probability within 5 and 10 millimeters when all other variables were held constant (Fig. 4, B and C). An illustrative example demonstrates spatial recurrence probability predictions. The patient's T1 post–gadolinium magnetic resonance imaging (MRI) scans are shown for three time points: (i) 24 hours before surgery, (ii) 48 hours after surgery, and (iii) 9-month surveillance MRI, which identified tumor recurrence (Fig. 4D). The patient's samples were then plotted along with a 3D representation of their original tumor. Spheres representative of the probability of recurrence within 5 (P5mm) and 10 mm (P10mm) of each sample were plotted (Fig. 4E). During initial tumor removal, sample 1, along the posterior margin, demonstrated an AI-infiltration of 0.60, P5mm 73%, and P10mm 87%. Sample 2, along the inferior margin, demonstrated an AI-infiltration of 0.94, P5mm 72%, and P10mm 90%. Sample 2 corresponded with imaging-defined recurrence.

Using AI-infiltration as a measure of recurrence enables actionable forecasting of future tumor growth sites at the earliest stages of diagnosis. Intraoperative SRH imaging of unprocessed samples requires a processing time of under 60 s per sample (*14*, *19*, *21*). Therefore, the use of this technology would allow for rapid, point-of-care testing (Fig. 4F). Together, these results suggest that optical histology of GBM infiltration, combined with clinical variables, may enable the estimation of focal recurrence before standard-of-care imaging.

DISCUSSION

GBM remains among the most challenging and universally fatal diagnoses due to frequent recurrence despite tumor resection, cytotoxic chemotherapy, radiation, and targeted molecular therapies. Recurrence occurs most often at the resection cavity margins (*4*). To localize the regional specificity of treatment failure, we tested and internally validated optical microscopy AI-infiltration models of recurrence in this study. This method for rapid quantification of tumor infiltration demonstrated the ability to predict focal recurrence of GBM using unprocessed tissue samples acquired during initial tumor removal from the resection cavity margins. These results will inform future precision medicine–targeted therapies for patients with late-stage disease.

Our findings demonstrated the relationship between malignant cell infiltration and the predictability of focal recurrence following chemoradiation. Noninvasive MRI has recently shown malignant infiltration and its correlation with GBM recurrence. Akbari *et al.* (*22*) used multiparametric MRI to generate surrogates for infiltration to produce predictions of focal recurrence, generating an mAUC of 84%. Further investigation determined that combined multiparametric regression using apparent diffusion coefficient with FLAIR signal intensity accurately estimated microscopic nonenhancing GBM burden and the regional heterogeneity of tumor recurrence (*23*). These studies, however, required imaging at the point of treatment failure, in contrast to recurrence models generated here representing tissue samples taken at the time of initial diagnosis, opening the possibility for intervention at the earliest stages of the disease.

Experimental multimodal regional therapies for patients with GBM recurrence, including dose escalation radiation and catheter-based chemotherapy delivery, have both been limited by an inability to target the highest-risk regions. Radiobiological theory suggests that optimal tumor control can be achieved when the dose delivered increases proportionately to the burden of malignant cells within the radiation field (*24*). This foundational principle resulted in numerous trials aimed at dose escalation radiotherapy, but many have shown minimal to no differences in overall survival for patients with GBM (*25*). Recent work using multiparametric and spectroscopy MRI to define hypercellular and infiltrative regions within and around GBM represents a promising innovation (*26*, *27*). The application of AI-infiltration may further refine and optimize radiation planning. Similarly, one major obstacle to adequately delivering regional cytotoxic, molecular, and vaccine therapies directly into GBM is defining where these drugs should be administered within large heterogeneous tumors (*28*, *29*). Imprecise targeting of glioma regions bearing the greatest extent of infiltration is one explanation for the mixed results of published clinical trials. AI-infiltration models defining a regional distribution of future recurrence could be incorporated into future clinical research applications.

Several limitations in this study may affect the interpretation of the results and its clinical application. The study protocol did not define a minimum number of samples or the sample distribution outside of attempts to sample from the widest distribution under a clinical context. While we believe that imaged tissues were regionally distributed without significant clustering, we cannot speak to the extent of GBM infiltration between sampled sites. Furthermore, while functional imaging and physiological brain mapping informed whether tumor margin samples could be acquired, proximity to eloquent areas of the brain limited our ability to obtain an unbiased representation of tumor biology across the entire resection margin and was not a recurrence model feature (*4*, *30*–*33*). Last, all patients included in both test and validation cohorts were treated with maximal resection; therefore, it remains unknown how the recurrence models presented would perform in patients with unresectable GBMs.

MATERIALS AND METHODS

Patient selection and study design

The entire patient cohort for this multicenter, retrospective cohort study was obtained from patients who had previously been recruited for intraoperative SRH imaging between March 2022 and March 2025. For the UCSF cohort, more than 400 patients and 2200 samples were analyzed between March 2022 and January 2024, of which a nested subpopulation of 60 patients with 273 samples were included in the training cohort of this study. Inclusion criteria included any patient age greater than 18 with pathology-confirmed IDH–wild-type GBM that had intraoperative SRH imaging performed at the time of resection. Using the same criteria, a UCSF test cohort was identified for internal validation, comprising 20 patients with 98 samples who underwent resection and intraoperative SRH imaging between February and July 2024. The study was approved by the Human Research Protection Program Institutional Review Board (IRB) of the UCSF, and all patients provided informed consent for study inclusion (UCSF IRB # 17-23215).

Patient demographics and clinical information

Demographic, clinical, histopathological, and radiographic information for all 60 UCSF patients in the training cohort and all 20 patients in the testing cohort were obtained retrospectively via electronic medical records. Demographic variables included age and sex. Clinical variables collected were primary or recurrent status at time of surgery, as well as outcomes data regarding time to progression, death, and follow-up. Pathology reports were used to confirm IDH–wild-type GBM diagnosis as well as proliferation index. Further tumor characteristics were identified using UCSF500 targeted next generation sequencing, which provided tumor mutational burden, methylation score, and molecular features such as chromosomal abnormalities, gene deletions, amplifications, and fusions.

Quantification of preoperative and postoperative tumor volumes was performed using 3D Slicer as an image computing platform version 5.8.0 (https://slicer.org/) (*3*). T1 post–gadolinium MRI scans obtained within 24 hours before resection were used for preoperative contrast-enhancing (CE) tumor volume assessment, and T2-FLAIR scans were used for preoperative flair volume assessment. T1 post–gadolinium MRI scans within 72 hours postresection were used for postoperative volume assessment. Manual segmentation was performed with region-of-interest analysis of CE regions to quantify tumor volume. Extent of resection was then calculated as (preoperative tumor volume − postoperative tumor volume) / preoperative tumor volume × 100%. To ensure that postoperative CE tumor measurements did not include blood products or other fluid collections, T1 pre–gadolinium and DWI imaging were used to subtract these regions from the region of interest. Multifocal or multicentric disease was defined as noncontiguous areas of disease based on T1-weighted postcontrast images or FLAIR sequences. All multifocal lesions were measured separately and summed together for a single volumetric measurement. Preoperative and postoperative MRI scans were available for all patients.

Follow-up imaging was used to assess for recurrence using RANO 2.0 guidelines. This incorporated the development of new or progressive contrast enhancement on follow-up imaging in the appropriate clinical context along with tumor board consensus. Patients with distant recurrence were not excluded given that the analysis was performed at the level of individual sample sites rather than at the patient level.

Sample selection and distribution

Intraoperatively, one sample was taken from the core of each patient's tumor, and following resection, samples were taken from the margins of the resection cavity. The sampling strategy aimed to obtain specimens from multiple orientations around the resection cavity (anterior, posterior, medial, lateral, superior, and inferior) when possible. With each sample taken, stereotactic coordinates were obtained along with screenshots of the sample location as identified on the Brainlab neuronavigation system. These unprocessed, fresh samples were then imaged using SRH, which generated an image that was analyzed at a pixel level and output an AI-generated infiltration value of 0 to 1. Follow-up imaging at recurrence time was cross-referenced with preoperative and postoperative imaging to assess for recurrence at the individual sample level. Using expert-guided manual inspection with the observers blinded to clinical results, sample sites were identified as recurred or not. Classification was performed using imaging from the patient's initial point of recurrence as determined by RANO 2.0 and the manual localization of each intraoperative margin sample site to determine its colocalization with new CE recurrence. Spatial localization of sampled sites on postoperative imaging did not demonstrate colocalization with regions of residual CE tumor at the time of initial resection.

Using each sample's stereotactic coordinates, Euclidean distance was calculated between each core sample (a proxy for core tumor location) and its respective margin samples. These distances were used to plot the samples in 3D space, allowing for a visual inspection of the sample distribution. Kernel density plots were generated using kernel density estimation in R with a Gaussian kernel and optimized bandwidth (bw = nrd0), and these were leveraged to assess sample distribution in each axis. Sample distribution variability was then assessed within each patient by calculating pairwise Euclidean distances and the SD between samples within a patient, which were then averaged for total sample variability per patient.

FastGlioma development and infiltration score generation

Methods for developing a model to detect and quantify glioma infiltration (FastGlioma) are fully outlined in previous work by Kondepudi *et al.* (*21*). In brief, a large and diverse dataset of SRH images was used to develop a visual foundation model through self-supervision training of a patch tokenizer and whole-slide encoder. These models were then fine-tuned using ordinal representation learning with a combined dataset of surgical specimens and corresponding SRH images. The FastGlioma model uses a linear slide scoring layer to output a single scalar value between 0 and 1 that indicates the degree of tumor infiltration within a whole-slide SRH image. Ordinal metric learning was subsequently implemented by a neuropathologist ranking the degree of tumor infiltration within each SRH image on a four-tier scale 0 to 3: 0 is normal brain tissue/no tumor, 1 is atypical cells/possible tumor, 2 is sparse tumor infiltration, and 3 is dense tumor infiltration. FastGlioma informed infiltration values were then validated in a prospective multicenter, international cohort of patients.

Classifier screening and training

Predictor screening was performed as an exploratory tool to understand potential signal from variables in the dataset and their association with recurrence. This was conducted using a bootstrap forest partitioning method. To improve generalizability and clinical applicability, variables that are routinely available in standard clinical practice were prioritized for final model building. These included clinical, radiographic, and molecular features obtained through chart review and radiographic segmentation in 3D slicer. R studio version 2024.12.0 was used to run a 10-fold internal stratified cross-validation using logistic regression, k-NN, SVMs, RF, GBTs, and XGB. Upsampling of the minority class was used within each cross-validation fold when training the models. Predictability was reported as the average AUC across folds plus/minus the SD. As the best performing model, RF models used Gini impurity for node splitting, with the number of variables randomly sampled at each split (mtry) optimized on the basis of AUC during cross-validation within the caret framework. Additional hyperparameter tuning using grid-based search across mtry and tree depth demonstrated minimal impact on model performance (ΔAUC <0.02), and therefore default parameter settings were retained. RF was then applied to the test cohort, with performance and generalizability assessed using the AUC and its 95% bootstrapped confidence interval based on 2000 resamples. The code for this model can be found on github (https://github.com/sanjeevherr/ForecastGlioma.git). Shapley additive explanations were then

calculated to determine the directionality and impact of each variable on the RF model. The minimum practical number of variables for predictor accuracy was identified through manual reverse elimination using a clinically accepted AUC cutoff value of 0.80.

Spatially resolved recurrence probability prediction

For each sample, it was annotated whether recurrence was within 5 or 10 mm or further from the sample. These distances were chosen given previous literature identifying recurrence along the resection cavity border as the most prevalent type of recurrence. The previously established RF model was then used to classify samples by their proximity to recurrence. Separate classifier models were built using 10-fold internal stratified cross-validation for prediction of recurrence within 5 mm and within 10 mm of each sample location. Partial dependency plots were generated by setting each variable other than AI-infiltration to the median value across patients and then plotting the probabilities of recurrence that correspond to all possible AI-infiltration values from 0 to 1 (https://github.com/sanjeevherr/ForecastGlioma.git).

A visual representation was created for one of the patients depicting a mask of their tumor before resection along with the sites of each sample taken along the resection cavity at time of surgery. Then, for each sample, the probability of recurrence within 5 mm and within 10 mm was plotted using color-coded spheres. Slicer version 5.8.0 was used to create the tumor segment mask. The segment was then uploaded into python and plotted in 3D space using the tumor surface and Delaunay triangulation. Each sample was plotted using its stereotactic coordinates. The 2D images of these plots were then captured, and Adobe Illustrator was used to optimize coloring of sample infiltration scores and probability predictions.

Statistical analysis

Descriptive statistics were analyzed to compare patients who recurred to those who did not. Normality was determined using Shapiro-Wilk testing using a P value < 0.05 to determine significant deviation from normal distribution. Continuous variables that were normally distributed were tested for significance using an independent t test, and nonnormally distributed variables were compared using Wilcoxon rank-sum testing. Categorical variables were tested for significance using Fisher's exact or chi-squared tests. All comparative analyses used P value < 0.05 to determine significance. All analyses were performed using R (Vienna, Austria) or GraphPad Prism version 10.2.3 (San Diego, CA)

Supplementary Materials

This PDF file includes:

Figs. S1 to S6

REFERENCES

1. P. Karschnia, J. S. Young, A. Dono, L. Häni, T. Sciortino, F. Bruno, S. T. Juenger, N. Teske, R. A. Morshed, A. F. Haddad, Y. Zhang, S. Stoecklein, M. Weller, M. A. Vogelbaum, J. Beck, N. Tandon, S. Hervey-Jumper, A. M. Molinaro, R. Rudà, L. Bello, O. Schnell, Y. Esquenazi, M. I. Ruge, S. J. Grau, M. S. Berger, S. M. Chang, M. van den Bent, J. C. Tonn, Prognostic validation of a new classification system for extent of resection in glioblastoma: A report of the RANO resect group. *Neuro Oncol.* **25**, 940–954 (2023).
2. T. J. Brown, M. C. Brennan, M. Li, E. W. Church, N. J. Brandmeir, K. L. Rakszawski, A. S. Patel, E. B. Rizk, D. Suki, R. Sawaya, M. Glantz, Association of the extent of resection with survival in glioblastoma: A systematic review and meta-analysis. *JAMA Oncol.* **2**, 1460–1469 (2016).
3. A. M. Molinaro, S. Hervey-Jumper, R. A. Morshed, J. Young, S. J. Han, P. Chunduru, Y. Zhang, J. J. Phillips, A. Shai, M. Lafontaine, J. Crane, A. Chandra, P. Flanigan, A. Jahangiri, G. Cioffi, Q. Ostrom, J. E. Anderson, C. Badve, J. Barnholtz-Sloan, A. E. Sloan, B. J. Erickson, P. A. Decker, M. L. Kosel, D. LaChance, J. Eckel-Passow, R. Jenkins, J. Vallanueva-Meyer, T. Rice, M. Wrensch, J. K. Wiencke, N. A. Oberheim Bush, J. Taylor, N. Butowski, M. Prados, J. Clarke, E. Chang, M. Aghi, P. Theodosopoulos, M. McDermott, M. S. Berger, Association of maximal extent of resection of contrast-enhanced and non-contrast-enhanced tumor with survival within molecular subgroups of patients with newly diagnosed glioblastoma. *JAMA Oncol.* **6**, 495–503 (2020).
4. P. Karschnia, A. Dono, J. S. Young, S. T. Juenger, N. Teske, L. Häni, T. Sciortino, C. Y. Mau, F. Bruno, L. Nunez, R. A. Morshed, A. F. Haddad, M. Weller, M. van den Bent, N. Thon, J. Beck, S. Hervey-Jumper, A. M. Molinaro, N. Tandon, R. Ruda, M. A. Vogelbaum, L. Bello, O. Schnell, S. J. Grau, S. M. Chang, M. S. Berger, Y. Esquenazi, J. C. Tonn, Associations between recurrence patterns and outcome in glioblastoma patients undergoing re-resection: A complementary report of the RANO resect group. *Neuro Oncol.* **26**, 584–586 (2024).
5. H. A. Shah, A. Mishra, M. J. Gouzoulis, N. Ben-Shalom, R. S. D'Amico, Analysis of factors leading to early termination in glioblastoma-related clinical trials. *J. Neurooncol* **158**, 489–495 (2022).
6. E. J. Smith, A. Naik, M. Goel, P. Y. Wen, M. Lim, S. M. Chang, I. M. Germano, Adult neuro-oncology trials in the United States over 5 decades: Analysis of trials completion rate to guide the path forward. *Neurooncol. Adv.* **6**, vdad169 (2024).
7. K. Petrecca, M. C. Guiot, V. Panet-Raymond, L. Souhami, Failure pattern following complete resection plus radiotherapy and temozolomide is at the resection margin in patients with glioblastoma. *J. Neurooncol* **111**, 19–23 (2013).
8. A. F. Kazerooni, H. Akbari, G. Shukla, C. Badve, J. D. Rudie, C. Sako, S. Rathore, S. Bakas, S. Pati, A. Singh, M. Bergman, S. M. Ha, D. Kontos, M. Nasrallah, S. J. Bagley, R. A. Lustig, D. M. O'Rourke, A. E. Sloan, J. S. Barnholtz-Sloan, S. Mohan, M. Bilello, C. Davatzikos, Cancer imaging phenomics via CaPTk: Multi-institutional prediction of progression-free survival and pattern of recurrence in glioblastoma. *JCO Clin. Cancer Inform.* **4**, 234–244 (2020).
9. A. A. Gal, P. T. Cagle, The 100-year anniversary of the description of the frozen section procedure. *JAMA* **294**, 3135–3137 (2005).
10. H. L. Somerset, B. K. Kleinschmidt-DeMasters, Approach to the intraoperative consultation for neurosurgical specimens. *Adv Anat Pathol* **18**, 446–449 (2011).
11. S. J. Robboy, S. Weintraub, A. E. Horvath, B. W. Jensen, C. B. Alexander, E. P. Fody, J. M. Crawford, J. R. Clark, J. Cantor-Weinberg, M. G. Joshi, M. B. Cohen, M. B. Prystowsky, S. M. Bean, S. Gupta, S. Z. Powell, V. O. Speights Jr., D. J. Gross, W. S. Black-Schaffer, Pathologist workforce in the United States: I. Development of a predictive model to examine factors influencing supply. *Arch. Pathol. Lab. Med.* **137**, 1723–1732 (2013).
12. R. K. Orosco, V. J. Tapia, J. A. Califano, B. Clary, E. E. W. Cohen, C. Kane, S. M. Lippman, K. Messer, A. Molinolo, J. D. Murphy, J. Pang, A. Sacco, K. R. Tringale, A. Wallace, Q. T. Nguyen, Positive surgical margins in the 10 most common solid cancers. *Sci. Rep.* **8**, 5686 (2018).
13. M. Ji, S. Lewis, S. Camelo-Piragua, S. H. Ramkissoon, M. Snuderl, S. Venneti, A. Fisher-Hubard, M. Garrard, D. Fu, A. C. Wang, J. A. Heth, C. O. Maher, N. Sanai, T. D. Johnson, C. W. Freudiger, O. Sagher, X. S. Xie, D. A. Orringer, Detection of human brain tumor infiltration with quantitative stimulated Raman scattering microscopy. *Sci. Transl. Med.* **7**, 309ra163 (2015).
14. D. A. Orringer, B. Pandian, Y. S. Niknafs, T. C. Hollon, J. Boyle, S. Lewis, M. Garrard, S. L. Hervey-Jumper, H. J. L. Garton, C. O. Maher, J. A. Heth, O. Sagher, D. A. Wilkinson, M. Snuderl, S. Venneti, S. H. Ramkissoon, K. A. McFadden, A. Fisher-Hubbard, A. P. Lieberman, T. D. Johnson, X. S. Xie, J. K. Trautman, C. W. Freudiger, S. Camelo-Piragua, Rapid intraoperative histology of unprocessed surgical specimens via fiber-laser-based stimulated Raman scattering microscopy. *Nat. Biomed. Eng.* **1**, 0027 (2017).
15. C. W. Freudiger, W. Min, B. G. Saar, S. Lu, G. R. Holtom, C. He, J. C. Tsai, J. X. Kang, X. S. Xie, Label-free biomedical imaging with high sensitivity by stimulated Raman scattering microscopy. *Science* **322**, 1857–1861 (2008).
16. D. G. Eichberg, A. H. Shah, L. Di, A. M. Semonche, G. Jimsheleishvili, E. M. Luther, C. A. Sarkiss, A. D. Levi, S. H. Gultekin, R. J. Komotar, M. E. Ivan, Stimulated Raman histology for rapid and accurate intraoperative diagnosis of CNS tumors: Prospective blinded study. *J. Neurosurg.* **134**, 137–143 (2019).
17. M. Pekmezci, R. A. Morshed, P. Chunduru, B. Pandian, J. Young, J. E. Villanueva-Meyer, T. Tihan, E. A. Sloan, M. K. Aghi, A. M. Molinaro, M. S. Berger, S. L. Hervey-Jumper, Detection of glioma infiltration at the tumor margin using quantitative stimulated Raman scattering histology. *Sci. Rep.* **11**, 12162 (2021).
18. T. C. Hollon, C. Jiang, A. Chowdury, M. Nasir-Moin, A. Kondepudi, A. Aabedi, A. Adapa, W. Al-Holou, J. Heth, O. Sagher, P. Lowenstein, M. Castro, L. I. Wadiura, G. Widhalm, V. Neuschmelting, D. Reinecke, N. von Spreckelsen, M. S. Berger, S. L. Hervey-Jumper, J. G. Golfinos, M. Snuderl, S. Camelo-Piragua, C. Frediger, H. Lee, D. A. Orringer, Artificial intelligence-based molecular classification of diffuse gliomas using rapid, label-free optical imaging. *Nat. Med.* **4**, 828–832 (2023).
19. T. C. Hollon, B. Pandian, A. R. Adapa, E. Urias, A. V. Save, S. S. S. Khalsa, D. G. Eichberg, R. S. D'Amico, Z. U. Farooq, S. Lewis, P. D. Petridis, T. Marie, A. H. Shah, H. J. L. Garton, C. O. Maher, J. A. Heth, E. L. McKean, S. E. Sullivan, S. L. Hervey-Jumper, P. G. Patil, B. G. Thompson, O. Sagher, G. M. McKhann II, R. J. Komotar, M. E. Ivan, M. Snuderl,

M. L. Otten, T. D. Johnson, M. B. Sisti, J. N. Bruce, K. M. Muraszko, J. Trautman, C. W. Freudiger, P. Canoll, H. Lee, S. Camelo-Piragua, D. A. Orringer, Near real-time intraoperative brain tumor diagnosis using stimulated Raman histology and deep neural networks. *Nat. Med.* **26**, 52–58 (2020).
20. T. C. Hollon, B. Pandian, E. Urias, A. V. Save, A. R. Adapa, S. Srinivasan, N. K. Jairath, Z. Farooq, T. Marie, W. N. Al-Holou, K. Eddy, J. A. Heth, S. S. S. Khalsa, K. Conway, O. Sagher, J. N. Bruce, P. Canoll, C. W. Freudiger, S. Camelo-Piragua, H. Lee, D. A. Orringer, Rapid, label-free detection of diffuse glioma recurrence using intraoperative stimulated Raman histology and deep neural networks. *Neuro Oncol.* **23**, 144–155 (2021).
21. A. Kondepudi, M. Pekmezci, X. Hou, K. Scotford, C. Jiang, A. Rao, E. S. Harake, A. Chowdury, W. Al-Holou, L. Wang, A. Pandey, P. R. Lowenstein, M. G. Castro, L. I. Koerner, T. Roetzer-Pejrimovsky, G. Widhalm, S. Camelo-Piragua, M. Movahed-Ezazi, D. A. Orringer, H. Lee, C. Freudiger, M. Berger, S. Hervey-Jumper, T. Hollon, Foundation models for fast, label-free detection of glioma infiltration. *Nature* **637**, 439–445 (2025).
22. H. Akbari, L. Macyszyn, X. Da, M. Bilello, R. L. Wolf, M. Martinez-Lage, G. Biros, M. Alonso-Basanta, D. M. O'Rourke, C. Davatzikos, Imaging surrogates of infiltration obtained via multiparametric imaging pattern analysis predict subsequent location of recurrence of glioblastoma. *Neurosurgery* **78**, 572–580 (2016).
23. P. D. Chang, D. S. Chow, P. H. Yang, C. G. Filippi, A. Lignelli, Predicting glioblastoma recurrence by early changes in the apparent diffusion coefficient value and signal intensity on FLAIR images. *AJR Am. J. Roentgenol.* **208**, 57–65 (2017).
24. G. S. Stamatakos, V. P. Antipas, N. K. Uzunoglu, R. G. Dale, A four-dimensional computer simulation model of the in vivo response to radiotherapy of glioblastoma multiforme: Studies on the effect of clonogenic cell density. *Br. J. Radiol.* **79**, 389–400 (2006).
25. R. E. Wegner, S. Abel, Z. D. Horne, S. Hasan, V. Verma, T. Ranjan, R. W. Williamson, S. M. Karlovits, National trends in radiation dose escalation for glioblastoma. *Radiat. Oncol. J.* **37**, 13–21 (2019).
26. M. M. Kim, Y. Sun, M. P. Aryal, H. A. Parmar, M. Piert, B. Rosen, C. S. Mayo, J. M. Balter, M. Schipper, N. Gabel, E. M. Briceño, D. You, J. Heth, W. Al-Holou, Y. Umemura, D. Leung, L. Junck, D. R. Wahl, T. S. Lawrence, Y. Cao, A phase 2 study of dose-intensified chemoradiation using biologically based target volume definition in patients with newly diagnosed glioblastoma. *Int. J. Radiat. Oncol. Biol. Phys.* **110**, 792–803 (2021).
27. K. Ramesh, E. A. Mellon, S. S. Gurbani, B. D. Weinberg, E. Schreibmann, S. A. Sheriff, M. Goryawala, M. de le Fuente, B. R. Eaton, J. Zhong, A. D. Voloschin, S. Sengupta, E. M. Dunbar, M. Holdhoff, P. B. Barker, A. A. Maudsley, L. R. Kleinberg, H. Shim, H. G. Shu, A multi-institutional pilot clinical trial of spectroscopic MRI-guided radiation dose escalation for newly diagnosed glioblastoma. *Neurooncol. Adv.* **4**, vdac006 (2022).
28. J. N. Sarkaria, L. S. Hu, I. F. Parney, D. H. Pafundi, D. H. Brinkmann, N. N. Laack, C. Giannini, T. C. Burns, S. H. Kizilbash, J. K. Laramy, K. R. Swanson, T. J. Kaufmann, P. D. Brown, N. Y. R. Agar, E. Galanis, J. C. Buckner, W. F. Elmquist, Is the blood-brain barrier really disrupted in all glioblastomas? A critical assessment of existing clinical data. *Neuro. Oncol.* **20**, 184–191 (2018).
29. R. S. D'Amico, M. K. Aghi, M. A. Vogelbaum, J. N. Bruce, Convection-enhanced drug delivery for glioblastoma: A review. *J. Neurooncol* **151**, 415–427 (2021).
30. E. F. Chang, A. Clark, J. S. Smith, M. Y. Polley, S. M. Chang, N. M. Barbaro, A. T. Parsa, M. W. McDermott, M. S. Berger, Functional mapping-guided resection of low-grade gliomas in eloquent areas of the brain: Improvement of long-term survival. *J. Neurosurg.* **114**, 566–573 (2011).
31. J. K. W. Gerritsen, M. L. D. Broekman, S. De Vleeschouwer, P. Schucht, B. V. Nahed, M. S. Berger, A. J. P. E. Vincent, Safe surgery for glioblastoma: Recent advances and modern challenges. *Neurooncol. Pract.* **9**, 364–379 (2022).
32. M. M. Grabowski, P. F. Recinos, A. S. Nowacki, J. L. Schroeder, L. Angelov, G. H. Barnett, M. A. Vogelbaum, Residual tumor volume versus extent of resection: Predictors of survival after surgery for glioblastoma. *J. Neurosurg.* **121**, 1115–1123 (2014).
33. R. L. Yong, T. Wu, N. Mihatov, M. J. Shen, M. A. Brown, K. A. Zaghloul, G. E. Park, J. K. Park, Residual tumor volume and patient survival following reoperation for recurrent glioblastoma. *J. Neurosurg.* **121**, 802–809 (2014).
34. C. Jiang, A. Chowdury, X. Hou, A. Kondepudi, C. W. Freudiger, K. Conway, S. Camelo-Piragua, D. A. Orringer, H. Lee, T. C. Hollon, OpenSRH: Optimizing brain tumor surgery using intraoperative stimulated Raman histology. *Adv. Neural Inf. Process. Syst.* **35**, 28502-28516 (2022).

Acknowledgments: We thank K. Probst and N. Sirivansanti for illustrator support. **Funding:** This work was supported by the following National Institute of Health (NIH) funding sources: NINDS R01 NS137950 (S.L.H.-J.) K12NS080223 (T.H.), and T32GM007863 (A.K.); Curci Foundation (S.L.H.-J.); NCI P01 CA118816 (S.L.H.-J.); Chan Zuckerberg Foundation (CZI) Advancing Imaging (T.H.); Cook Family Brain Tumor Research Fund (T.H.); Mark Trauner Brain Research Fund (T.H. and S.L.H.-J.); Zenkel Family Foundation (T.H and S.L.H.-J.); Ian's Friends Foundation (T.H.); Resonance Philanthropies (S.L.H.-J.); UM Precision Health Investigators Awards grant program (T.H.); Translational AI Award from the UM Department of Neurosurgery (T.H.); and UM Stanley and Judith Frankel Institute for Heart and Brain Health Innovative Multidisciplinary Research Pilot Award (T.H.) **Author contributions:** Each author's contribution(s) to the paper have been listed as follows: Conceptualization: S.H., S.L.H.-J., T.H., and M.P. Methodology: S.H., S.L.H.-J., T.H., Y.S., V.A., A.P., T.P., A.Ki., M.S., M.P., and A.D. Investigation: S.H., S.L.H.-J., T.H., N.O., K.S., A.P., T.P., A.Ko., M.S., M.P., A.Ki., G.M., G.V., J.P., J.M., A.M., B.K., G.W., and L.K. Visualization: S.H., S.L.H.-J., T.H., N.O., Y.S., K.S., T.P., A.Ko., M.S., M.P., and A. Ki. Funding acquisition: S.H., S.L.H.-J., T.H., and M.S.B. Project administration: S.H., S.L.H.-J., T.H., J.K., M.P., J.Y., and M.S.B. Supervision: S.H., S.L.H.-J., T.H., M.S., M.P., N.A.O.-B., A.Ki., J.Y., and M.S.B. Writing—original draft: S.H., S.L.H.-J., T.H., M.P., N.A.O.-B., A.Ki., J.Y., and M.S.B. Writing—review and editing: S.H., S.L.H.-J., T.H., N.O., J.K., Y.S., V.A., K.S., A.P., T.P., A.Ko., M.S., M.P., N.A.O.-B., A.Ki., J.Y., M.S.B., and A.D. **Competing interests:** The authors declare that they have no competing interests. **Data, code, and materials availability:** All model parameters will be publicly available for investigational use only under a Creative Commons Attribution Non-Commercial Share Alike 4.0 license. Model parameters are available at Github (https://github.com/sanjeev-herr/ForecastGlioma.git) and at Zenodo (https://doi.org/10.5281/zenodo.22802244). Restrictions apply to the availability of raw patient imaging or genetic data, which were used with institutional permission through IRB approval for the current study and are, therefore, not publicly available. All data and code needed to evaluate and reproduce the results in the paper are present in the paper and/or the Supplementary Materials. All data sharing between medical centers, including deidentified raw patient imaging or genetic data, is regulated through data use agreements with the study authors. A similar data-sharing protocol may be established for interested investigators pending scientific review. Data can be shared only for noncommercial academic purposes and will require a formal material transfer agreement. Please contact UCSF (datasharing@ucsf.edu) for any requests for data sharing. All requests will be evaluated based on institutional and departmental policies to determine whether the data requested are subject to intellectual property or patient privacy obligations. Upon evaluation of the request, the data transfer agreement will then be initiated by the study institution to the requesting institution. Public access to an open-source repository of SRH images can be found at OpenSRH (https://opensrh.mlins.org/). Stimulated Raman histology images used in the figures of this manuscript were obtained from the OpenSRH dataset (*34*), available at https://opensrh.mlins.org/. OpenSRH data are distributed under the Creative Commons Attribution-NonCommercial-ShareAlike 4.0 International License (CC BY-NC-SA 4.0; https://creativecommons.org/licenses/by-nc-sa/4.0/).

Submitted 8 October 2025
Accepted 18 August 2026
Published 25 September 2026
10.1126/sciadv.aec8202

ScienceAdvances

Optical microscopy predictions of focal recurrence in glioblastoma

Sanjeev Herr, Niels Olshausen, Melike Pekmezci, Jasleen Kaur, Youssef Sibih, Vardhaan Ambati, Abraham Dada, Katie Scotford, Amit Persad, Thiebaud Picart, Akhil Kondepudi, Gabrielle Malte, Gabriella Vulakh, Johanna Pechmann, Jessica Makolli, Nancy Ann Oberheim-Bush, Albert Kim, Jacob Young, Mitchel S. Berger, Ammar Mallouhi, Barbara Kiesel, Georg Widhalm, Lisa Körner, Madhumita Sushil, Todd Hollon, and Shawn L. Hervey-Jumper

Sci. Adv. **12** (39), eaec8202. DOI: 10.1126/sciadv.aec8202